



1 **Exploring the amplified role of HCHO during the wintertime ozone**
2 **and PM_{2.5} pollution in a coastal city of southeast China**

3 Youwei Hong^{a,b,c,d,g*}, Keran Zhang^{a,b,d}, Dan Liao^f, Gaojie Chen^{a,b,c}, Min Zhaoⁱ, Yiling Lin^{a,b,e},
4 Xiaoting Ji^{a,b,c}, Ke Xu^{a,b,g}, Yu Wu^{a,b,e}, Ruilian Yu^e, Gongren Hu^e, Sung-Deuk Choi^h, Likun Xue^{i*},
5 Jinsheng Chen^{a,b,c}

6

7 ^aCenter for Excellence in Regional Atmospheric Environment, Key Lab of Urban Environment and
8 Health, Institute of Urban Environment, Chinese Academy of Sciences, Xiamen, 361021, China

9 ^bFujian Key Laboratory of Atmospheric Ozone Pollution Prevention, Institute of Urban
10 Environment, Chinese Academy of Sciences, Xiamen, 361021, China

11 ^cUniversity of Chinese Academy of Sciences, Beijing, 100049, China

12 ^dCollege of Resources and Environment, Fujian Agriculture and Forest University, Fuzhou 350002,
13 China

14 ^eCollege of Chemical Engineering, Huaqiao University, Xiamen, 361021, China

15 ^fCollege of Environment and Public Health, Xiamen Huaxia University, Xiamen 361024, China

16 ^gSchool of Life Sciences, Hebei University, Baoding, 071000, China

17 ^hDepartment of Urban and Environmental Engineering, Ulsan National Institute of Science and
18 Technology, Ulsan, 44919, South Korea

19 ⁱEnvironment Research Institute, Shandong University, Qingdao, 266237, China

20

21 *Corresponding author E-mail: Youwei Hong (ywhong@iue.ac.cn); Likun Xue
22 (xuelikun@sdu.edu.cn)

23

24

25

26

27

28



29 **Abstract:**

30 To develop the effective strategies for controlling both PM_{2.5} and O₃ levels, it is crucial
31 to understand their synergistic mechanisms, key precursors, and atmospheric
32 physiochemical processes involved. In this study, a wintertime co-occurring O₃ and
33 PM_{2.5} pollution event in a coastal city in southeast China was investigated based on
34 high-time resolution measurements of criteria air pollutants, chemical compositions of
35 PM_{2.5}, and O₃ precursors, such as NO_x, HCHO, and VOCs. The results of this study
36 revealed a positive correlation between PM_{2.5} and MDA8 O₃ concentrations during the
37 whole periods, suggesting an increase in atmospheric oxidation capacity (AOC) during
38 the cold seasons. Strong correlations ($R^2 = 0.415\text{--}0.477$) were observed between
39 HCHO, Fe, Mn, and sulfate concentrations, suggesting the influence of catalyzed
40 oxidation processes in the coastal city. Through an observation-based model (OBM)
41 analysis coupled with the regional atmospheric chemistry mechanism version 2
42 (RACM2) and the chemical aqueous-phase radical mechanism version 3.0 (CAPRAM
43 3.0), we found that high concentrations of precursors (SO₂ and HCHO), high relative
44 humidity, and moderately acidic pH conditions enhanced the heterogeneous formation
45 of hydroxymethanesulfonate (HMS) in PM_{2.5}. Furthermore, by employing the Master
46 Chemical Mechanism (OBM-MCM), we verified that disabling the HCHO mechanism
47 could decrease daytime net O₃ production rates by reducing the production rates of
48 HO₂+NO. These results were consistent with the daily values of AOC, OH, HO₂, and
49 RO₂ concentrations. This study contributes to a better understanding of the significance



50 of HCHO in photochemical reactions and the formation of secondary aerosols in a
51 coastal city.

52 **Key words:** PM_{2.5}; O₃; formaldehyde; OBM; coastal city

53

54 **Introduction**

55 Air pollution, dominated by fine particulate matter (PM_{2.5}) and ground-level ozone
56 (O₃), is an important global environmental issue linked to climate change and human
57 health, including cardiovascular and respiratory illnesses and mortality (Xiao et al.,
58 2022; Vohra et al., 2022). To decrease global air pollution and associated mortality, the
59 World Health Organization recently updated its air quality guideline for annual PM_{2.5}
60 exposure from 10 to 5 µg m⁻³ and added the average O₃ concentrations of no more than
61 60 µg m⁻³ during the peak season (WHO, 2021). To develop two-pollutant control
62 strategies to decrease both PM_{2.5} and O₃, there is a need to understand the synergistic
63 mechanisms and spatiotemporal delineation between them (Ivatt et al., 2022; Li et al.,
64 2019b).

65 There are complex synergistic effects between PM_{2.5} and O₃, due to common
66 precursors (e.g., NO_x and VOCs), atmospheric physiochemical processes, and weather
67 systems (Li et al., 2019a; Shao et al., 2022; Jia et al., 2023; Zhang et al., 2022; Qin et
68 al., 2021; Qu et al., 2023). Some studies have reported that O₃ could enhance the
69 formation of secondary PM_{2.5} by strengthening atmospheric oxidation capacity (Qin et
70 al., 2022; Zhao et al., 2020). An increase in O₃ concentration will increase oxidizing



71 substances, such as OH, H₂O₂, and RCHO, which promote the oxidation of SO₂, NO_x,
72 and VOCs to secondary inorganic and organic components in PM_{2.5} (Feng et al., 2020;
73 Lu et al., 2019). On the contrary, PM_{2.5} could affect O₃ formation by interfering with
74 the radiation intensity of the Earth, providing a multiphase reaction surface and
75 affecting the radiation flux and intensity of the boundary layer (Shao et al., 2021; Li et
76 al., 2017). In addition, multiphase reactions occur on the surface of atmospheric
77 particles, such as the hydrolysis of N₂O₅ and HO₂ absorption, thus affecting the
78 formation of O₃ precursors NO₂ (Song et al., 2022; Lou et al., 2014).

79 Formaldehyde (HCHO) plays an important role in the photochemical reaction
80 process and secondary aerosol formation (Kalashnikov et al., 2022; Ma et al., 2020;
81 Song et al., 2021; Zong et al., 2021). Most studies have focused on pollution
82 characteristics and sources, particle uptake of HCHO, and their impacts on atmospheric
83 oxidation capacity (Liu et al., 2022b; Wu et al., 2023; Zhang et al., 2021). Recent
84 studies have reported that atmospheric HCHO contributes to sulfate formation in PM_{2.5}
85 by producing HO₂ radicals and hydroxymethyl hydroperoxide (HMHP) or
86 hydroxymethanesulfonate (HMS) (Wu et al., 2023; Dovrou et al., 2022; Campbell et
87 al., 2022). These studies highlight the necessity for more observation research to obtain
88 evidence of the contributions of HCHO to HMS formation. However, in subtropical
89 coastal regions with apparent HCHO production, further studies are required to
90 investigate the impacts of HCHO on the synergistic effects between PM_{2.5} and O₃.

91 Xiamen, a coastal city in southeast China, has frequently experienced PM_{2.5}
92 pollution (with low O₃ concentrations) in winter and O₃ pollution in spring and autumn



93 (Hong et al., 2022; Wu et al., 2019). Our previous studies mainly focused on the
94 pollution characteristics of PM_{2.5} or O₃ in different seasons and their sources associated
95 with anthropogenic emissions and the East Asian monsoon (Liu et al., 2020; Liu et al.,
96 2022a; Hong et al., 2021). At the end of winter and the beginning of spring in 2022, an
97 outbreak of co-occurring O₃ and PM_{2.5} pollution was observed in Xiamen. Therefore,
98 it provided a unique opportunity to study the interactions among precursors,
99 heterogeneous chemistry, and photochemical reactions for the synergistic effects of
100 PM_{2.5} and O₃. In the coastal region, there is an apparent alternation of polluted and clean
101 air masses from continental and ocean areas and a local geographical environment,
102 including relatively high humidity, dense vegetation, and strong atmospheric oxidation
103 capacity (Hu et al., 2022; Wu et al., 2020). Potential synergistic mechanisms between
104 O₃ and PM_{2.5} would differ from those in megacities of China, such as the Beijing-
105 Tianjin-Hebei (BTH) Area, the Yangtze River Delta (YRD), and the Pearl River Delta
106 (PRD). Based on the observation-based model (OBM) analysis, the objectives of this
107 study are to (1) characterize the wintertime co-occurring O₃ and PM_{2.5} pollution process
108 in a coastal city; (2) elaborate the influence of HCHO on the heterogeneous formation
109 of hydroxymethanesulfonate (HMS) in PM_{2.5}; (3) explore the mechanisms of HCHO
110 on O₃ pollution and photochemical reactions process.

111

112 **2 Methods and materials**

113 **2.1 Study area**



114 The monitoring site (Institute of Urban Environment, Chinese Academy of
115 Sciences, 118.06° E, 24.61° N) is located in Xiamen, a coastal city in southeast China
116 (Fig. S1). It is situated in a subtropical monsoon climate, with an annual average
117 temperature of 23.3°C and a relative humidity of 77.6%. In autumn and winter, cold
118 and dry air masses move northward from inland, while in late spring and summer, the
119 prevailing air masses are southerly, characterized by warm air temperatures and high
120 humidity. The air-monitoring supersite is located on the rooftop of a building,
121 surrounded by residential buildings, educational institutions, a commercial zone, and
122 freeways. The downtown area of Xiamen, with a high population density and frequent
123 traffic jams, is located south of the monitoring site.

124

125 **2.2 Observation**

126 Gas and aerosol species, O₃ precursors, photolysis rate, and meteorological
127 parameters were continuously measured online from February 17 to March 17, 2022.
128 Hourly mass concentrations of PM_{2.5} and PM₁₀ were measured using a tapered element
129 oscillating microbalance (TEOM1405, Thermo Scientific Corp., MA, USA). NO/NO₂,
130 SO₂, and O₃ were monitored using continuous gas analyzers (TEI 42*i*, 43*i*, and 49*i*,
131 Thermo Scientific Corp., MA, USA). HCHO analyzer (FMS-100, Focused Photonics
132 Inc., Hangzhou, China) was used to measure gaseous HCHO based on the Hantzsch
133 reaction, according to our previous method (Liu et al., 2022b). Water-soluble inorganic
134 ions (WSII) in PM_{2.5} (Cl⁻, SO₄²⁻, NO₃⁻, Na⁺, K⁺, NH₄⁺, Mg²⁺, and Ca²⁺) were measured
135 hourly using a Monitoring device for AeRosols and Gases in ambient Air (MARGA



136 2080; Metrohm Applikon B.V.; Delft, Netherlands). Simultaneously, organic carbon
137 (OC) and elemental carbon (EC) in PM_{2.5} were measured using an OC/EC analyzer
138 (model RT-4; Sunset Laboratory Inc.; Tigard, USA). BC was monitored using an
139 Aethalometer (AE31, Magee Scientific, USA) with a PM_{2.5} cut-off inlet. Besides,
140 concentrations of 22 elements (Al, Si, S, Fe, K, Mn, Pb, Ca, Zn, Ba, V, Cu, Ni, As, Cr,
141 Ag, Se, Br, Hg, Sn, Ti, and Sb) were measured using a multi-metal monitor (Xact™
142 625, Cooper Environmental Services, LLT; Portland, USA). Strict quality assurance
143 and quality control procedures were applied, and the maintenance and accuracy of all
144 online instruments were validated (Hong et al., 2021).

145 A gas chromatograph-mass spectrometer (GC-FID/MS, TH-300B, Wuhan, China)
146 was used to measure ambient VOCs with one-hour time resolution, following the
147 method from our previous studies (Liu et al., 2020a,b). Briefly, the air sample was
148 preconcentrated by cooling to -160 °C in a cryogenic trap, then heated to 100 °C, and
149 subsequently transferred to the secondary trap using high-purity helium (He). The low-
150 carbon (C₂-C₅) hydrocarbons were detected using a flame ionization detector (FID)
151 with a PLOT (Al₂O₃/KCl) column (15 m × 0.32 mm × 6.0 μm), while other VOC
152 species were quantified using a GC/MS with a DB-624 column (60 m × 0.25 mm × 1.4
153 μm). The instrument can quantify 106 VOC species, including 29 alkanes, 11 alkenes,
154 one alkyne, 17 aromatics, 35 halogenated hydrocarbons, and 13 OVOCs. Calibration
155 was performed daily at 23:00 using the standard mixtures of US EPA PAMS and TO-
156 15. The detection limits of the measured VOCs ranged from 0.02 ppbv to 0.30 ppbv.

157 Ambient meteorological parameters, including relative humidity (RH),



158 temperature (T), wind speed (WS), and wind direction (WD), were obtained using an
159 ultrasonic anemometer (150WX, Airmar, USA). Photolysis frequencies and HCHO
160 were measured using a photolysis spectrometer PFS-100 and a formaldehyde monitor
161 FMS-100 (Focused Photonics Inc., Hangzhou, China), respectively. The photolysis rate
162 constants include $J(\text{O}^1\text{D})$, $J(\text{NO}_2)$, $J(\text{H}_2\text{O}_2)$, $J(\text{HONO})$, $J(\text{HCHO})$, and $J(\text{NO}_3)$. The
163 distribution of fire spots during the observation periods was obtained from the Fire
164 Information for Resource Management System
165 (<https://firms.modaps.eosdis.nasa.gov/firemap/>). The data for boundary layer height
166 (BLH) were obtained from the European Centre for Medium-Range Weather Forecasts
167 (ECMWF) ERA5 hourly reanalysis dataset
168 (<https://www.ecmwf.int/en/forecasts/datasets/reanalysis-datasets/era5>, last access:
169 March 24, 2023).

170

171 2.3 Positive matrix factorization (PMF) analysis

172 The PMF 5.0 model was applied to quantify high-time-resolution sources of $\text{PM}_{2.5}$
173 during the observation periods. The details of the model analysis were described in our
174 previous studies (Hong et al., 2021; Liu et al., 2020). Briefly, Eq. (1) demonstrates j
175 compound species in the i th sample as the concentration from p independent sources.

$$176 \quad x_{ij} = \sum_{k=1}^p g_{ik} f_{kj} + e_{ij} \quad (1)$$

177 Where e_{ij} is the residual for each species, f_{kj} is the fraction of the j th species from
178 the k th source, g_{ik} is the species contribution of the k th source to the i th sample, x_{ij} is



179 the j th species concentration measured in the i th sample, and p is the total number of
180 independent sources. The Q value (Eq. (2)), based on the uncertainties (μ), was used to
181 evaluate the steadiness of the solution.

$$Q = \sum_{i=1}^n \sum_{j=1}^m \left[\frac{x_{ij} - \sum_{k=1}^p g_{ik} f_{kj}}{\mu_{ij}} \right]^2 \quad (2)$$

182
183

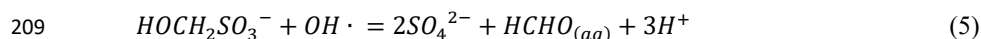
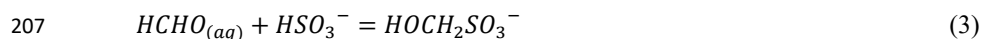
184 2.4 Observation-based model (OBM)

185 The OBM-MCM model is employed to simulate in situ atmospheric
186 photochemical processes and quantify the O_3 production rate, AOC, and OH reactivity.
187 The details of the OBM-MCM model were reported in our previous studies (Liu et al.,
188 2022a,b). In summary, monitoring data with a one-hour time resolution of air pollutants
189 (i.e., O_3 , CO, NO, NO_2 , HONO, SO_2 , and VOCs), meteorological parameters (i.e., T, P,
190 and RH), and photolysis rate constants ($J(O^1D)$, $J(NO_2)$, $J(H_2O_2)$, $J(HONO)$, $J(HCHO)$,
191 and $J(NO_3)$) were input into the OBM-MCM model as constraints for the model
192 simulation. The photolysis rates of other molecules were determined by solar zenith
193 angle and scaled using measured JNO_2 values (Saunders et al., 2003). The model
194 incorporates the physical process of deposition within the boundary layer height (BLH),
195 which varies from 300 m during nighttime to 1500 m during the daytime in autumn (Li
196 et al., 2018). Therefore, dry deposition velocities were used to simulate the deposition
197 loss of certain reactants in the atmosphere (Zhang et al., 2003; Xue et al., 2014).

198 To simulate the concentration of particulate HCHO and its role in the
199 heterogeneous formation of hydroxymethanesulfonate (HMS), we combined the OBM



200 model with the regional atmospheric chemistry mechanism version 2 (RACM2) and
201 the chemical aqueous-phase radical mechanism version 3.0 (CAPRAM 3.0). We also
202 considered the mass transfer processes between the gas and aqueous phases (Schwartz,
203 1986). The Henry's law constant of HCHO is $0.31 \times 10^8 \text{ M atm}^{-1}$, as estimated by
204 Mitsubishi et al. (2018). For the aqueous HMS formation mechanisms, dissolved HCHO
205 reacts with sulfite and bisulfite to form HMS (Eq (3-4)), which can be further oxidized
206 by aqueous OH radicals (Eq (5)).



210 The observation data of gaseous NO, NO₂, O₃, SO₂, CO, HCHO, VOCs,
211 particulate phase NO₃⁻, NH₄⁺, and Cl⁻, along with meteorological parameters with a 1-
212 h time resolution were interpolated to constrain the model, while the measured SO₄²⁻
213 was used as the initial condition for the model simulation. Liquid water content (LWC)
214 and aqueous H⁺ concentrations, calculated using the ISORROPIA-II model (Hong et
215 al., 2022), were also used to constrain the model. Model calculations were conducted
216 from February 26 to March 16, 2022. For each case, the model was initiated at 00:00
217 local time (LT), and the integration had a step of 1 h and a duration of 24 h.

218

219 2.5 Backward trajectory analysis

220 Hybrid Single-Particle Lagrangian Integrated Trajectory (HYSPLIT) was used to



221 analyze the air masses before and during the PM_{2.5} and O₃ pollution period. The 72-h
222 backward trajectories at a height of 100 m obtained from the National Oceanic and
223 Atmospheric Administration were run every hour. Cluster analysis was performed, and
224 four clusters were determined based on the total spatial variance (TSV).

225

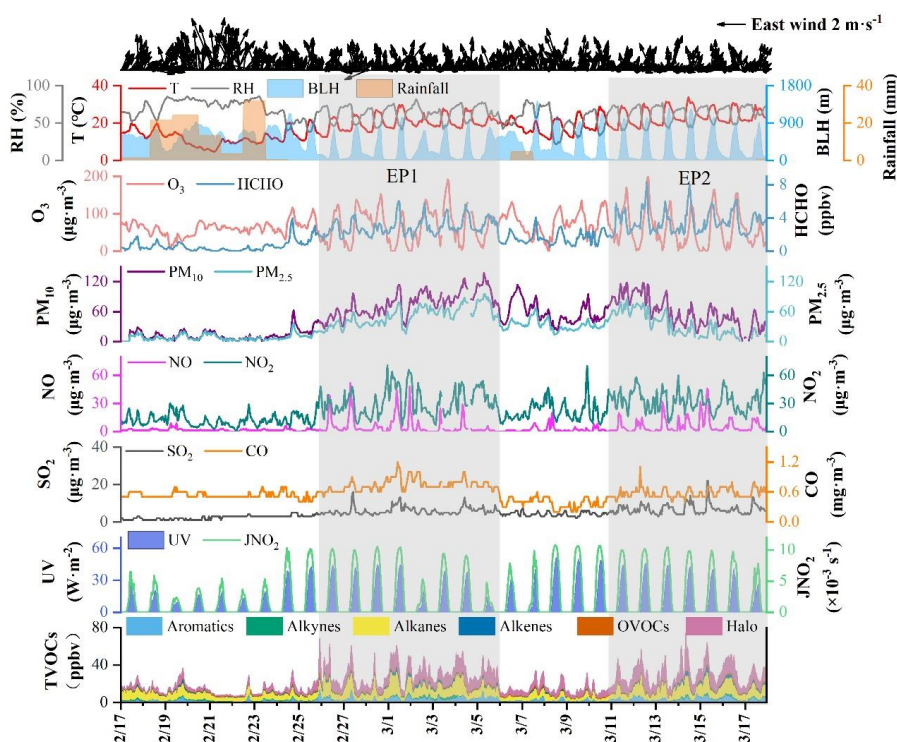
226 **3 Results and discussions**

227 **3.1 Overview of co-occurring O₃ and PM_{2.5} pollution**

228 The time series of criteria air pollutants, O₃ precursors, and meteorological
229 parameters from February 17 to March 17, 2022 are shown in Fig. 1. Two typical PM_{2.5}
230 and O₃ pollution episodes (EP1: February 26 to March 5; EP2: March 11 to March 17)
231 were observed, compared to the other periods (Pre-EP1: February 11 to February 25
232 and Pre-EP2: March 16 to March 10) affected by rainfall. The mean concentrations of
233 PM_{2.5} during EP1 and EP2 were 51.9 μg m⁻³ and 35.3 μg m⁻³, respectively, compared
234 to 9.03 μg m⁻³ during Pre-EP1 (Table S1). The concentrations of other air pollutants,
235 such as O₃, SO₂, NO₂, PM₁₀, OC, EC, BC, HCHO, and VOCs, showed a significant
236 increasing trend during EP1 and EP2. The maximum PM_{2.5} and O₃ concentrations were
237 approximately 100 μg m⁻³ and 200 μg m⁻³, respectively. The maximum daily 8 h
238 average (MDA8) O₃ concentrations were calculated according to the Ambient Air
239 Quality Standard of China. Fig. S2 shows the positive correlation between PM_{2.5} and
240 MDA8 O₃ concentrations during the whole period. In Xiamen, a coastal city in
241 Southeast China, the annual mean concentrations of criteria air pollutants from 2015 to



242 2021 were significantly lower than in other Chinese cities (Fig. S3) (Li et al., 2022;
 243 Shao et al., 2022). Therefore, these two typical PM_{2.5} and O₃ pollution episodes (EP1
 244 and EP2) might be worth exploring in terms of the formation mechanisms and
 245 synergistic effects of PM_{2.5} and O₃ in the coastal city.



246

247 **Fig. 1. Time series of various air pollutants and meteorological parameters**

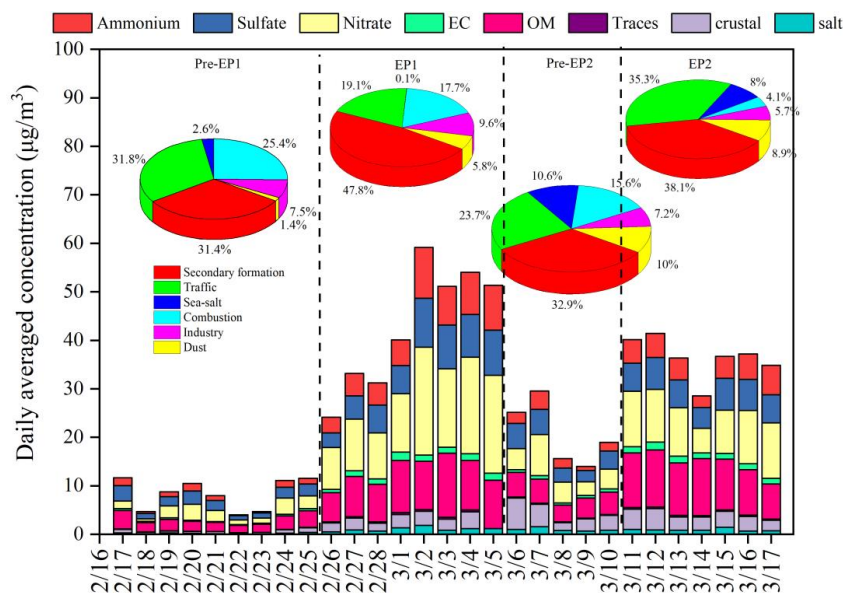
248

249 **3.2 Chemical compositions and sources of PM_{2.5}**

250 As shown in Figure 2, an overall increasing trend is clearly observed in both bulk
 251 PM_{2.5} and its major components during EP1 and EP2. Nitrate and organic matter (OM)
 252 remain the top two dominant PM_{2.5} components, followed by sulfate and ammonium.



253 The mean concentrations of SO_4^{2-} , NO_3^- , and NH_4^+ during EP1 and EP2 were $7.07 \mu\text{g}$
 254 m^{-3} and $5.87 \mu\text{g m}^{-3}$, $14.95 \mu\text{g m}^{-3}$ and $9.69 \mu\text{g m}^{-3}$, and $6.77 \mu\text{g m}^{-3}$ and $4.46 \mu\text{g m}^{-3}$,
 255 respectively (Table S1). The increase in EC indicates the contributions of local
 256 anthropogenic emission sources, such as vehicle exhausts (Fig. 2). The concentrations
 257 and percentages of OC and EC during different periods are illustrated in Fig. S4 and
 258 Table S1. The average OC and EC concentrations during EP1 and EP2 were $6.36 \mu\text{g}$
 259 m^{-3} and $7.48 \mu\text{g m}^{-3}$ and $1.23 \mu\text{g m}^{-3}$ and $1.29 \mu\text{g m}^{-3}$, respectively, which were notably
 260 higher than those during Pre-EP1 and Pre-EP2. These results are consistent with the
 261 increase in primary emissions and secondary formation contributing to complex air
 262 pollution during the rapid urbanization and industrialization stages in China (Xiao et
 263 al., 2022; Jiang et al., 2022).



264

265 **Fig. 2. Time series of $\text{PM}_{2.5}$ chemical composition and sources apportionment by the PMF**
 266 **model. In the legends, OM refers to organic matter, calculated as $1.4 \times \text{OC}$; “Tracers” includes**
 267 **elements other than Na, Cl, S, K, Al, Si, Ca, Fe; “Crustal” represents crustal materials,**



268 **calculated as $1.89 \times \text{Al} + 2.14 \times \text{Si} + 1.4 \times \text{Ca} + 1.43 \times \text{Fe}$; and “Salts” includes Na^+ and Cl^- .**

269 The PMF model was applied to conduct high-time-resolution source
270 apportionment of $\text{PM}_{2.5}$, based on online hourly measurement data (Hong et al., 2021;
271 Chow et al., 2022). The factor profiles and the contributions of various sources to $\text{PM}_{2.5}$
272 are shown in Fig. 2 and Fig. S5. Previous studies have indicated that construction and
273 road dust is characterized by high loadings of Al, Si, Ca^{2+} , Na^+ , Mg^{2+} , and Zn (Rianda
274 and Alves, 2021). In this study, the factor of dust (Factor 1) was identified by the high
275 contributions of Si (Fig. S5). The PMF analysis revealed that the contribution of dust
276 to $\text{PM}_{2.5}$ ranged from 5.8% to 8.9% during EP1 and EP2, compared to 1.4% during Pre-
277 EP1 (Fig.2). Factor 2, contributing to the high loading of metal elements (Mn, Zn, Fe,
278 Pb, and As), was characterized by industrial emissions (Belis et al., 2019). The
279 contributions from the industry during EP1 and EP2 remained constant. In factor 3, K^+
280 was dominant, and it was identified as coming from combustion sources (Watson et al.,
281 2001). Biomass burning could change the contribution of combustion to $\text{PM}_{2.5}$ at the
282 monitoring site through long-range transport. During EP2, the influence of combustion
283 sources (e.g., biomass burning) significantly decreased, due to reduced anthropogenic
284 emissions and the arrival of clean air masses from the ocean (Figs. S6 and S7). Factor
285 4, with the highest proportion of Na^+ and Mg^{2+} loadings, was associated with the
286 influence of sea-salt aerosol (Polissar et al., 1998). The percentages of sea salt (8-10%)
287 during Pre-EP2 and EP2 were relatively high. Factor 5 exhibited high contributions of
288 EC, OM, and Pb, which are general indicators of vehicle exhaust (Belis et al., 2019).
289 During EP2, the contribution of traffic increased up to 35.3%. Factor 6 was associated



290 with secondary aerosol, characterized by high loadings of SO_4^{2-} , NO_3^- , and NH_4^+ . The
291 increased contributions of secondary formation during EP1 and EP2 accounted for 47.8%
292 and 38.1%, respectively.

293

294 **3.3 Formation mechanism of $\text{PM}_{2.5}$**

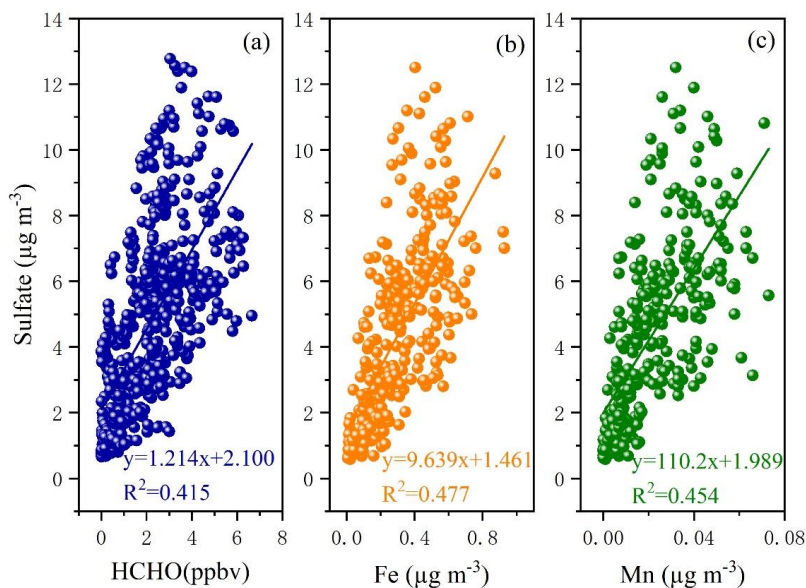
295 As shown in Fig. S8, SO_4^{2-} was correlated with NH_4^+ ($R^2 = 0.72\text{--}0.88$), and the
296 line fit of NH_4^+ and SO_4^{2-} showed a slope of 1.78-2.67, suggesting the dominant form
297 of $(\text{NH}_4)_2\text{SO}_4$. Similarly, NO_3^- was also correlated with NH_4^+ ($R^2 = 0.77\text{--}0.93$),
298 indicating the presence of NH_4NO_3 . In addition, the ratio of NH_4^+ to the sum of NO_3^-
299 and SO_4^{2-} was close to 1, indicating complete neutralization of sulfate and nitrate by
300 ammonium (Fig. 8c). However, there was no significant difference in the existing form
301 of SNA in $\text{PM}_{2.5}$ under different periods.

302 The variations of SOR and NOR under different periods are shown in Table S1. It
303 should be noted that SOR (0.38 ± 0.18) and NOR (0.32 ± 0.08) during EP1 were the
304 highest, indicating a high oxidation rate of SO_2 and NO_2 . According to RH, T, and UV
305 (Table S1), noticeable differences in meteorological conditions were observed under
306 different periods. In this study, LWC was positively correlated with SO_4^{2-} , NO_3^- , and
307 NH_4^+ (known as the secondary inorganic aerosol, SIA) (Fig. S9), suggesting the
308 influence of the aqueous phase process, including reactions with O_3 , OH, H_2O_2 , and
309 organic peroxides (Gen et al., 2019; Wang et al., 2023).

310 Current studies have found that O_3 , H_2O_2 , OH, and transition-metal-catalyzed
311 (TMI) O_2 can trigger the secondary formation of SO_4^{2-} (Hong et al., 2021; Gen et al.,



312 2019). However, the relative importance of these oxidants in enhancing the formation
313 of SO_4^{2-} is still a topic of debate. As shown in Fig. 3(b) and (c), a good correlation was
314 found between SO_4^{2-} and Fe and Mn. The TMI-catalyzed oxidation contributed to the
315 formation of SO_4^{2-} , which occurred in both cloud processes and during haze episodes
316 (Li et al., 2020) because the Mn catalytic reaction rapidly occurred at the aerosol surface
317 and could oxidize S(IV) through the production of intermediate Mn(III) (Wang et al.,
318 2021). Even at very low concentrations of Mn, the Mn catalytic reaction, consuming
319 oxygen and SO_2 , could produce sulfate. In addition, as an important intermediate
320 product in atmospheric photochemical reactions, the formation and removal of HCHO
321 are closely related to OH and HO_2 radicals, which directly affect atmospheric reactivity
322 and oxidation ability (Wu et al., 2023; Zhang et al., 2021). In this study, the correlations
323 ($R^2 = 0.415$) between HCHO and sulfate concentrations were also examined, as
324 displayed in Fig. 3(a). Recent studies have shown that HCHO can react with hydrogen
325 peroxide (H_2O_2) to produce hydroxymethyl hydroperoxide, which rapidly oxidizes
326 dissolved sulfur dioxide (SO_2 , aq) to sulfate (Dovrou et al., 2022). Meanwhile, HCHO
327 reacts with dissolved SO_2 (aq) to produce hydroxymethanesulfonate (HMS), which,
328 upon oxidation with the hydroxyl radical (OH), forms sulfate (Ma et al., 2020; Moch et
329 al., 2020).



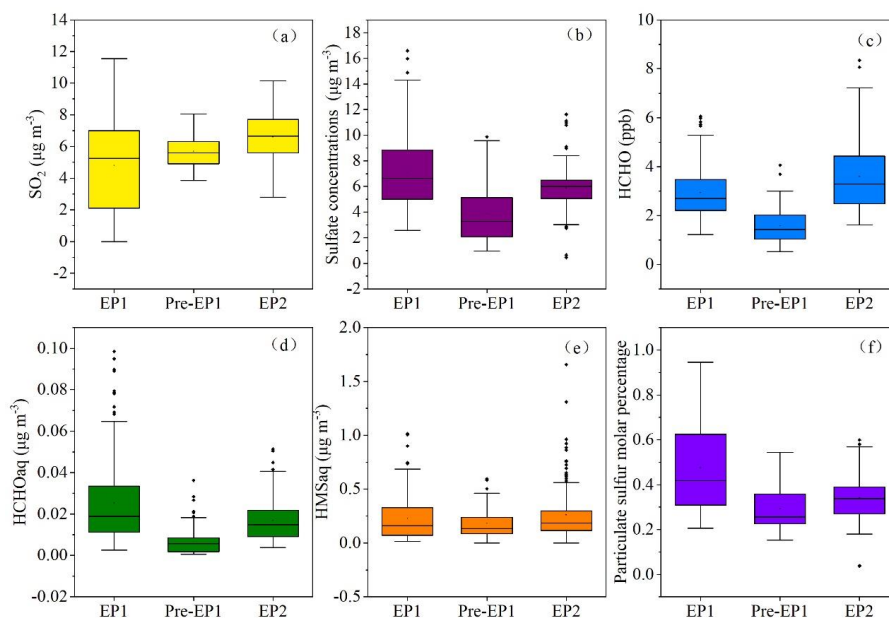
330

331 **Fig.3. Correlations between the concentrations of sulfate and HCHO (a), Fe (b), and Mn (c)**

332

333 3.4 Effects of HCHO on HMS in $\text{PM}_{2.5}$

334 To calculate the particulate concentrations of HCHO and its contributions to the
335 heterogeneous formation of HMS, we combined the OBM model with RACM2 and
336 CAPRAM 3.0. During EP1 and EP2, the concentrations of HCHO (aq) and HMS (aq),
337 as well as the particulate sulfur molar percentage, increased with the rise of SO_2 , SO_4^{2-} ,
338 and HCHO concentrations (Fig. 4). The increase in sulfate concentration was associated
339 with the increase in LWC (Fig. S9). Previous studies indicated that the pH and liquid
340 water content of aerosols were the main factors influencing the HCHO uptake
341 coefficient (γ). Moreover, γ has a strong positive exponential relationship with aqueous
342 sulfate concentration (Xu et al., 2022).

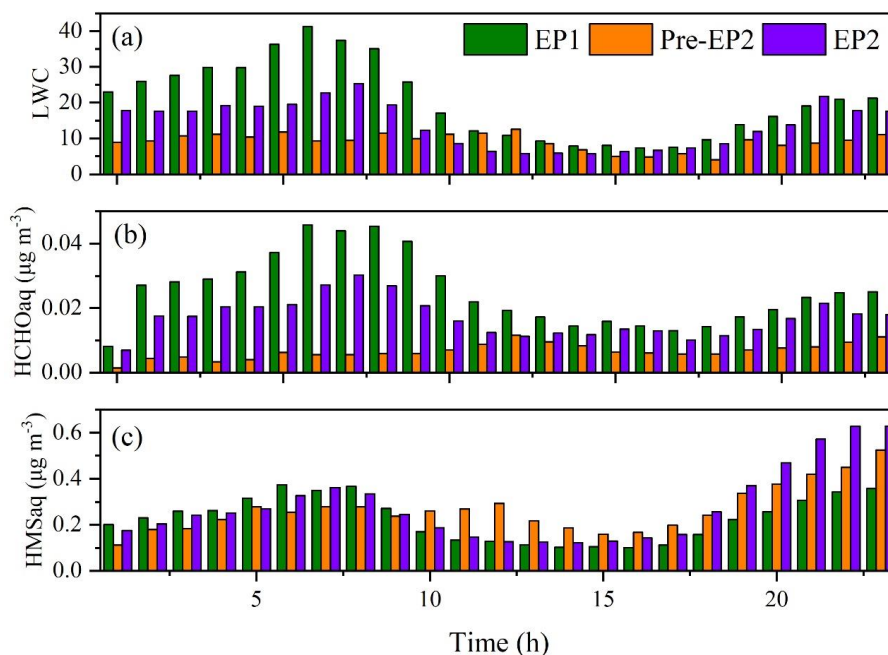


343

344 **Figure 4. Concentrations of SO_2 , SO_4^{2-} , HCHO, HCHO (aq), HMS (aq), and particulate sulfur**
 345 **molar percentage at different pollution levels. In the box-whisker plots, the whiskers, boxes,**
 346 **and points indicate the 5th/95th, 25th/75th, 50th percentiles, and mean values. The particulate**
 347 **sulfur molar percentage was calculated as $[\text{n}(\text{SO}_4^{2-})+\text{n}(\text{HMS})]/[\text{n}(\text{SO}_4^{2-})+\text{n}(\text{HMS})+\text{n}(\text{SO}_2)]$.**

348

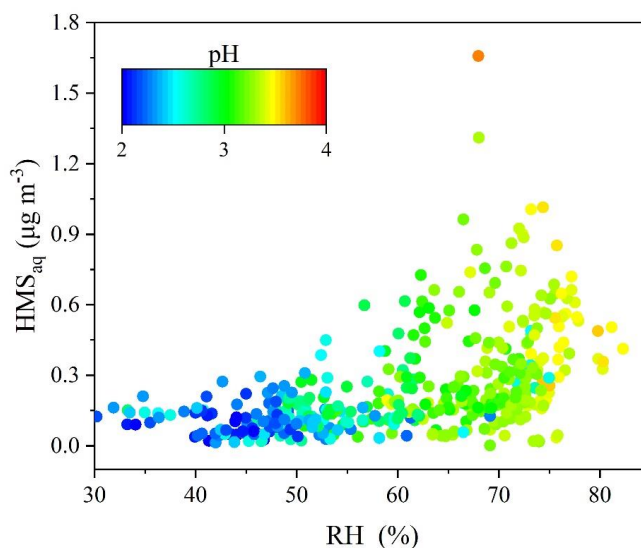
As shown in Fig. 5, the concentration of HMS exhibited a similar diurnal variation
 349 to that of HCHO (aq). These findings are consistent with the fact that HMS is formed
 350 through the reaction between dissolved SO_2 and formaldehyde (HCHO) in aerosol
 351 liquid water. In our previous studies, we observed that gaseous HCHO showed an
 352 increasing trend after sunrise, peaking at noon due to photochemical reactions (Liu et
 353 al., 2022b). However, during EP1 and EP2, high concentrations of HCHO (aq) were
 354 observed during nighttime. Meanwhile, the heterogeneous formation of HMS also
 355 occurred, resulting in elevated HMS concentrations during nighttime.



356

357 **Figure 5. Diurnal variations of calculated HCHO (aq) and HMS (aq) at different pollution**
 358 **levels**

359 In this study, high concentrations of HMS were observed under high RH and
 360 moderately acidic pH conditions (Fig. 6). Previous studies have also indicated that high
 361 RH promotes rapid HMS formation during winter haze, as the aerosol water content
 362 could provide numerous reaction interfaces for HMS formation (Ma et al., 2020).
 363 Meanwhile, atmospheric sulfur tended to distribute into the particle phase with
 364 increasing RH. Fig. 6 shows that HMS formation is favored under pH conditions close
 365 to 4.0. Previous studies reported that high HMS concentrations were found under
 366 moderate-pH conditions, as low pH inhibits HMS formation, and high pH is unsuitable
 367 for its preservation (Ma et al., 2020; Campbell et al., 2022). Therefore, the combination
 368 of high precursor concentrations (SO₂ and HCHO), high RH, and moderately acidic pH
 369 enhanced the heterogeneous formation of HMS in this coastal city.



370

371 **Figure 6. Evolution of HMS (aq) distribution with increasing RH, colored according to**
372 **aerosol pH.**

373

374 3.5 Effects of HCHO on O₃ formation

375 To investigate the effects of HCHO on O₃ formation during the co-occurring O₃

376 and PM_{2.5} pollution period, the OBB was used to quantify the detailed O₃ production

377 and loss pathways in both scenarios: input HCHO (IH) and non-input HCHO (NIH)

378 (Fig. 7 and Fig. S10). The daytime production rates of HO₂+NO and RO₂+NO in the

379 IH scenario were calculated to be 6.84 and 1.25 ppbv h⁻¹ for EP1 and 9.91 and 2.17

380 ppbv h⁻¹ for EP2, respectively. Meanwhile, the predominant O₃ loss reaction in this

381 scenario was OH+NO₂, with rates of 2.26 ppbv h⁻¹ for EP1 and 3.17 ppbv h⁻¹ for EP2,

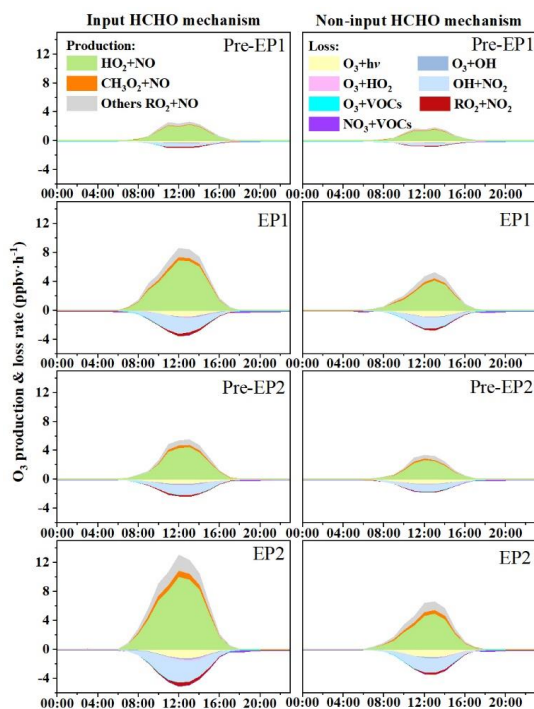
382 followed by O₃ photolysis with rates of 0.77 ppbv h⁻¹ and 1.10 ppbv h⁻¹. In contrast,

383 the daytime production rates of HO₂+NO and RO₂+NO in the NIH scenario were 4.03

384 and 0.85 ppbv h⁻¹ for EP1 and 4.86 and 1.29 ppbv h⁻¹ for EP2, respectively. These



385 results indicate that disabling the HCHO mechanism reduced the production rates of
 386 HO₂+NO by 41% for EP1 and 51% for EP2. In addition, the average maximum net O₃
 387 production rate observed with the IH scenario was 5.02 ppb h⁻¹ for EP1 and 7.93 ppb
 388 h⁻¹ for EP2, approximately two times higher than the values of 2.48 ppb h⁻¹ and 3.14
 389 ppb h⁻¹ observed with the NIH scenario. The results showed that the daytime net O₃
 390 production rates decreased by 50–60% when the HCHO mechanism was disabled,
 391 probably due to the decrease in ROx concentrations and radical propagation rates (Wu
 392 et al., 2023; Zhang et al., 2021).



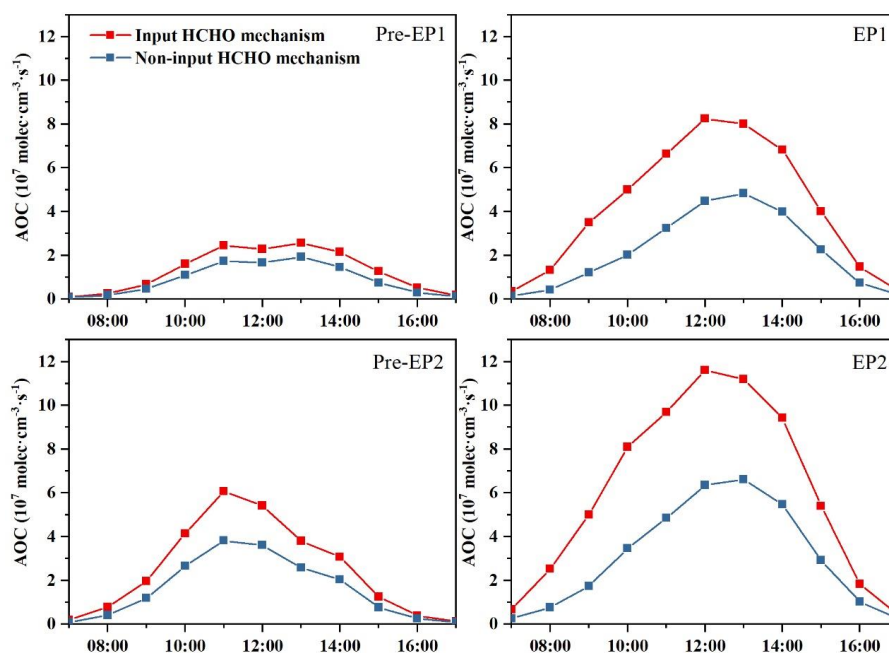
393

394 **Figure 7. O₃ production and loss rates by the OBM with and without the HCHO mechanism**

395 The atmospheric oxidation capacity (AOC) is a critical factor in determining the
 396 production rate of secondary pollutants and atmospheric photochemical pollution (Jia



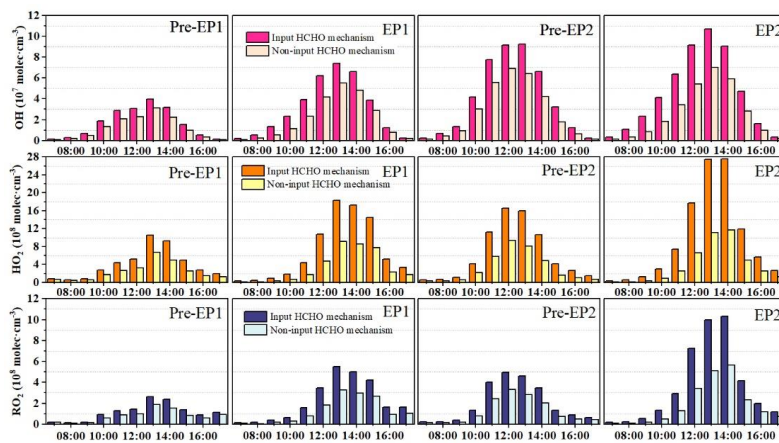
397 et al., 2023; Qin et al., 2022). In this study, AOC is calculated as the sum of the oxidation
398 rates of various primary pollutants (e.g., CO, NO_x, and VOCs) by major oxidants (i.e.,
399 OH, O₃, and NO₃). The model-simulated AOC, OH, HO₂, and RO₂ under different
400 periods are shown in Fig. 8 and Fig. 9. The daily maximum AOC during EP1 and EP2
401 was 8.24×10^7 and 11.6×10^7 molecules cm⁻³ s⁻¹, respectively, which were higher than
402 those (2.56×10^7 and 5.39×10^7 molecules cm⁻³ s⁻¹) in other periods. However, when the
403 HCHO mechanism was disabled, the daily maximum AOC during different stages
404 decreased significantly. Especially, HCHO played much important role in AOC during
405 the co-occurring PM_{2.5} and O₃ pollution periods. All these results are comparable to rural
406 sites in Hong Kong (6.2×10^7) and Berlin (1.4×10^7 molecules cm⁻³ s⁻¹) but lower than
407 those observed in highly polluted cities, such as Santiago (3.2×10^8 molecules cm⁻³ s⁻¹)
408 and Shanghai (1.0×10^8 molecules cm⁻³ s⁻¹) (Li et al., 2018; Xue et al., 2016; Liu et al.,
409 2022a). These studies have reported that the variations in AOC are related to precursor
410 concentrations/types and photochemical conditions.



411

412 **Figure 8. Atmospheric oxidation capacity (AOC) calculated by the OBM with and without**
 413 **the HCHO mechanism.**

414 In addition, the maximum daily concentrations of OH, HO₂, and RO₂ exhibited a
 415 similar pattern to that of AOC in both the IH and NIH scenarios (Fig. 9). Therefore, the
 416 O₃ production rate during EP1 and EP2 was consistent with the maximum daily values
 417 of AOC, OH, HO₂, and RO₂. The differences in RO_x levels between the IH and NIH
 418 model scenarios were also calculated (Fig. S11). In this study, disabling the HCHO
 419 mechanism led to decreased RO_x concentrations, affecting the O₃ formation. These
 420 results highlight the significance of HCHO in the photochemical reactions occurring in
 421 the coastal city during the co-occurring O₃ and PM_{2.5} pollution period.



422

423

Figure 9. OH, HO₂, and RO₂ concentrations modeled by the OBM with or without the HCHO mechanism

424

425

426



427

428 **Conclusions**

429 A wintertime co-occurring O₃ and PM_{2.5} pollution event was selected to investigate
430 the synergistic effects between PM_{2.5} and O₃ in a coastal city in southeast China. The
431 results demonstrated a positive correlation between PM_{2.5} and MDA8 O₃
432 concentrations during the whole periods, indicating the enhancement of atmospheric
433 oxidation capacity (AOC) during cold seasons. The result of positive matrix
434 factorization (PMF) analysis suggested that the contribution of secondary formation to
435 PM_{2.5} increased during the pollution events, implying that the elevated AOC promoted
436 the oxidation of SO₂, NO_x, and VOCs, leading to the formation of secondary inorganic
437 and organic components. We also observed significant correlations ($R^2 = 0.415\text{--}0.477$)
438 between HCHO, Fe, Mn, and sulfate concentrations, suggesting the influence of
439 catalyzed oxidation in the coastal city. Through OBM analysis, we demonstrated that
440 high concentrations of precursors (SO₂ and HCHO), high RH, and moderately acidic
441 pH conditions enhanced the heterogeneous formation of hydroxymethanesulfonate
442 (HMS). Meanwhile, we verified that the input HCHO mechanism increased the
443 concentrations of RO_x and net O₃ production rates. Moreover, the production rates of
444 HO₂+NO and RO₂+NO were enhanced, indicating that HCHO affected O₃ formation
445 by controlling the efficiencies of radical propagation. This study highlighted the
446 influence of the HCHO mechanism on co-occurring O₃ and PM_{2.5} pollution in coastal
447 cities and was beneficial for improving air quality and protecting public health.

448



449 **Data Availability.** The data set related to this work can be accessed via
450 <https://doi.org/10.5281/zenodo.7799302> (Hong, 2023). The details are also available
451 upon request from the corresponding author (ywhong@iue.ac.cn).

452

453

454 **Authorship Contribution Statement.** YW designed and wrote the manuscript. YL and
455 LD collected the data, and GJ and ZM contributed to the modeling analyses. KR, XT,
456 XK, and WY performed data analysis. SD, LK, RL, and GR contributed to revising the
457 manuscript. JS supported funding of observation and research.

458

459 **Competing interests.** The authors declare that they have no conflict of interest.

460

461 **Acknowledgement.** The authors gratefully acknowledge Yanting Chen and Zhiqian
462 Shao (Institute of Urban Environment, Chinese Academy of Sciences) for their
463 guidance and assistance during the observation, and Lingling Xu, Mengren Li, and
464 Xiaolong Fan (Institute of Urban Environment, Chinese Academy of Sciences) for the
465 discussion of this paper. This research was supported by the Xiamen Atmospheric
466 Environment Observation and Research Station of Fujian Province (Institute of Urban
467 Environment, Chinese Academy of Sciences).

468

469 **Financial support.** This research was financially supported by the National Natural
470 Science Foundation of China (42277091, U22A20578), the foreign cooperation
471 project of Fujian Province (2020I0038), the Xiamen Youth Innovation Fund Project
472 (3502Z20206094), the FJIRSM&IUE Joint Research Fund (RHZX-2019-006), and
473 Center for Excellence in Regional Atmospheric Environment project (E0L1B20201).

474

475



476 References

- 477 Belis, C. A., Pikridas, M., Lucarelli, F., Petralia, E., Cavalli, F., Calzolari, G., Berico, M., and Sciare, J.:
478 Source apportionment of fine PM by combining high time resolution organic and inorganic chemical
479 composition datasets, *Atmos. Environ.-X*, 3, 10.1016/j.aeaoa.2019.100046, 2019.
- 480 Campbell, J. R., Battaglia, M., Dingilian, K., Cesler-Maloney, M., St Clair, J. M., Hanisco, T. F.,
481 Robinson, E., DeCarlo, P., Simpson, W., Nenes, A., Weber, R. J., and Mao, J.: Source and Chemistry
482 of Hydroxymethanesulfonate (HMS) in Fairbanks, Alaska, *Environ. Sci. Technol.*,
483 10.1021/acs.est.2c00410, 2022.
- 484 Chow, W. S., Liao, K., Huang, X. H. H., Leung, K. F., Lau, A. K. H., and Yu, J. Z.: Measurement report:
485 The 10-year trend of PM_{2.5} major components and source tracers from 2008 to 2017 in an urban
486 site of Hong Kong, China, *Atmos. Chem. Phys.*, 22, 11557-11577, 10.5194/acp-22-11557-2022,
487 2022.
- 488 Dovrou, E., Bates, K. H., Moch, J. M., Mickley, L. J., Jacob, D. J., and Keutsch, F. N.: Catalytic role of
489 formaldehyde in particulate matter formation, *P. Natl. Acad. Sci. USA*, 119, e2113265119,
490 10.1073/pnas.2113265119, 2022.
- 491 Feng, T., Zhao, S., Zhang, X., Wang, Q., Liu, L., Li, G., and Tie, X.: Increasing wintertime ozone levels
492 and secondary aerosol formation in the Guanzhong basin, central China, *Sci. Total Environ.*, 745,
493 10.1016/j.scitotenv.2020.140961, 2020.
- 494 Gen, M., Zhang, R., Huang, D. D., Li, Y., and Chan, C. K.: Heterogeneous SO₂ Oxidation in Sulfate
495 Formation by Photolysis of Particulate Nitrate, *Environ. Sci. Technol. Letters*, 6, 86-91,
496 10.1021/acs.estlett.8b00681, 2019.
- 497 Hong, Y., Xu, X., Liao, D., Zheng, R., Ji, X., Chen, Y., Xu, L., Li, M., Wang, H., Xiao, H., Choi, S.-D.,
498 and Chen, J.: Source apportionment of PM_{2.5} and sulfate formation during the COVID-19
499 lockdown in a coastal city of southeast China, *Environ. Pollut.*, 286, 117577,
500 <https://doi.org/10.1016/j.envpol.2021.117577>, 2021.
- 501 Hong, Y., Xu, X., Liao, D., Liu, T., Ji, X., Xu, K., Liao, C., Wang, T., Lin, C., and Chen, J.: Measurement
502 report: Effects of anthropogenic emissions and environmental factors on the formation of biogenic
503 secondary organic aerosol (BSOA) in a coastal city of southeastern China, *Atmos. Chem. Phys.*, 22,



- 504 7827-7841, 10.5194/acp-22-7827-2022, 2022.
- 505 Hong, youwei. (2023). Dataset for ACP by Hong et al., 2023 [Data set]. Zenodo. 584
506 <https://doi.org/10.5281/zenodo.7799302>.
- 507 Hu, B., Duan, J., Hong, Y., Xu, L., Li, M., Bian, Y., Qin, M., Fang, W., Xie, P., and Chen, J.: Exploration
508 of the atmospheric chemistry of nitrous acid in a coastal city of southeastern China: results from
509 measurements across four seasons, *Atmos. Chem. Phys.*, 22, 371-393, 10.5194/acp-22-371-2022,
510 2022.
- 511 Ivatt, P. D., Evans, M. J., and Lewis, A. C.: Suppression of surface ozone by an aerosol-inhibited
512 photochemical ozone regime, *Nat. Geosci.*, 10.1038/s41561-022-00972-9, 2022.
- 513 Jia, C., Tong, S., Zhang, X., Li, F., Zhang, W., Li, W., Wang, Z., Zhang, G., Tang, G., Liu, Z., and Ge,
514 M.: Atmospheric oxidizing capacity in autumn Beijing: Analysis of the O₃ and PM_{2.5} episodes
515 based on observation-based model, *J Environ. Sci.*, 124, 557-569,
516 <https://doi.org/10.1016/j.jes.2021.11.020>, 2023.
- 517 Jiang, Y., Wang, S., Xing, J., Zhao, B., Li, S., Chang, X., Zhang, S., and Dong, Z.: Ambient fine
518 particulate matter and ozone pollution in China: Synergy in anthropogenic emissions and
519 atmospheric processes, *Environ. Res. Lett.*, 2022.
- 520 Kalashnikov, D. A., Schnell, J. L., Abatzoglou, J. T., Swain, D. L., and Singh, D.: Increasing co-
521 occurrence of fine particulate matter and ground-level ozone extremes in the western United States,
522 *Sci. Adv.*, 8, 10.1126/sciadv.abi9386, 2022.
- 523 Li, Zhanqing, Guo, Jianping, Ding, Aijun, Liao, Hong, Liu, and Jianjun: Aerosol and boundary-layer
524 interactions and impact on air quality, *Nat. Sci. Rev.*, 2017.
- 525 Li, J., Zhang, Y.-L., Cao, F., Zhang, W., Fan, M., Lee, X., and Michalski, G.: Stable Sulfur Isotopes
526 Revealed a Major Role of Transition-Metal Ion-Catalyzed SO₂ Oxidation in Haze Episodes,
527 *Environ. Sci. Technol.*, 54, 2626-2634, 10.1021/acs.est.9b07150, 2020.
- 528 Li, K., Jacob, D. J., Liao, H., Shen, L., Zhang, Q., and Bates, K. H.: Anthropogenic drivers of 2013-2017
529 trends in summer surface ozone in China, *P. Natl. Acad. Sci. USA of the United States of America*,
530 116, 422-427, 10.1073/pnas.1812168116, 2019a.
- 531 Li, K., Jacob, D. J., Liao, H., Zhu, J., Shah, V., Shen, L., Bates, K. H., Zhang, Q., and Zhai, S.: A two-
532 pollutant strategy for improving ozone and particulate air quality in China, *Nat. Geosci.*, 12, 906-+,



- 533 10.1038/s41561-019-0464-x, 2019b.
- 534 Li, Y., Zhang, Z., and Xing, Y.: Long-Term Change Analysis of PM_{2.5} and Ozone Pollution in China's
535 Most Polluted Region during 2015-2020, *Atmosphere*, 13, 10.3390/atmos13010104, 2022.
- 536 Li, Z., Xue, L., Yang, X., Zha, Q., Tham, Y. J., Yan, C., Louie, P. K. K., Luk, C. W. Y., Wang, T., and
537 Wang, W.: Oxidizing capacity of the rural atmosphere in Hong Kong, Southern China, *Sci. Total
538 Environ.*, 612, 1114-1122, <https://doi.org/10.1016/j.scitotenv.2017.08.310>, 2018.
- 539 Liu, T., Clegg, S. L., and Abbatt, J. P. D.: Fast oxidation of sulfur dioxide by hydrogen peroxide in
540 deliquesced aerosol particles, *P. Natl. Acad. Sci. USA*, 117, 1354-1359, 10.1073/pnas.1916401117,
541 2020a.
- 542 Liu, T., Hu, B., Yang, Y., Li, M., Hong, Y., Xu, X., Xu, L., Chen, N., Chen, Y., Xiao, H., and Chen, J.:
543 Characteristics and source apportionment of PM_{2.5} on an island in Southeast China: Impact of sea-
544 salt and monsoon, *Atmos. Res.*, 235, 10.1016/j.atmosres.2019.104786, 2020.
- 545 Liu, T., Hong, Y., Li, M., Xu, L., Chen, J., Bian, Y., Yang, C., Dan, Y., Zhang, Y., Xue, L., Zhao, M.,
546 Huang, Z., and Wang, H.: Atmospheric oxidation capacity and ozone pollution mechanism in a
547 coastal city of southeastern China: analysis of a typical photochemical episode by an observation-
548 based model, *Atmos. Chem. Phys.*, 22, 2173-2190, 10.5194/acp-22-2173-2022, 2022a.
- 549 Liu, T., Lin, Y., Chen, J., Chen, G., Yang, C., Xu, L., Li, M., Fan, X., Zhang, F., and Hong, Y.: Pollution
550 mechanisms and photochemical effects of atmospheric HCHO in a coastal city of southeast China,
551 *Sci. Total Environ.*, 160210, <https://doi.org/10.1016/j.scitotenv.2022.160210>, 2022b.
- 552 Lou, S., Liao, H., and Zhu, B.: Impacts of aerosols on surface-layer ozone concentrations in China
553 through heterogeneous reactions and changes in photolysis rates, *Atmos. Environ.*, 85, 123-138,
554 <https://doi.org/10.1016/j.atmosenv.2013.12.004>, 2014.
- 555 Lu, K., Guo, S., Tan, Z., Wang, H., Shang, D., Liu, Y., Li, X., Wu, Z., Hu, M., and Zhang, Y.: Exploring
556 atmospheric free-radical chemistry in China: the self-cleansing capacity and the formation of
557 secondary air pollution, *Nat. Sci. Rev.*, 6, 579-594, 2019.
- 558 Ma, T., Furutani, H., Duan, F., Kimoto, T., Jiang, J., Zhang, Q., Xu, X., Wang, Y., Gao, J., Geng, G., Li,
559 M., Song, S., Ma, Y., Che, F., Wang, J., Zhu, L., Huang, T., Toyoda, M., and He, K.: Contribution
560 of hydroxymethanesulfonate (HMS) to severe winter haze in the North China Plain, *Atmos. Chem.
561 Phys.*, 20, 5887-5897, <https://doi.org/10.5194/acp-20-5887-2020>, 2020.



- 562 Mitsuishi, K.; Iwasaki, M.; Takeuchi, M.; Okochi, H.; Kato, S.; Ohira, S. I.; Toda, K., Diurnal
563 Variations in Partitioning of Atmospheric Glyoxal and Methylglyoxal between Gas and
564 Particles at the Ground Level and in the Free Troposphere. *Acs Earth and Space Chemistry*
565 2018, 2, (9), 915-924.
- 566 Moch, J. M.; Dovrou E., Mickley L. J., Keutsch F. N., Liu Z., Wang Y., et al. Global Importance of
567 Hydroxymethanesulfonate in Ambient Particulate Matter: Implications for Air Quality. *J*
568 *Geophys. Res.-Atmospheres* 2020, 125(18),1-14
- 569 Moch, J. M., Dovrou, E., Mickley, L. J., Keutsch, F. N., Liu, Z., Wang, Y., Dombek, T. L., Kuwata,
570 M., Budisulistiorini, S. H., Yang, L., Decesari, S., Paglione, M., Alexander, B., Shao, J.,
571 Munger, J. W., and Jacob, D. J.: Global Importance of Hydroxymethanesulfonate in Ambient
572 Particulate Matter: Implications for Air Quality, *J Geophys. Res.-Atmospheres*, 125,
573 10.1029/2020jd032706, 2020
- 574 Polissar, A. V., Hopke, P. K., and Paatero, P.: Atmospheric aerosol over Alaska - 2. Elemental composition
575 and sources, *J Geophys. Res.-Atmospheres*, 103, 19045-19057, 10.1029/98jd01212, 1998.
- 576 Qin, M., Hu, A., Mao, J., Li, X., Sheng, L., Sun, J., Li, J., Wang, X., Zhang, Y., and Hu, J.: PM_{2.5} and
577 O₃ relationships affected by the atmospheric oxidizing capacity in the Yangtze River Delta, China,
578 *Sci. Total Environ.*, 810, 152268, <https://doi.org/10.1016/j.scitotenv.2021.152268>, 2022.
- 579 Qin, Y., Li, J., Gong, K., Wu, Z., Chen, M., Qin, M., Huang, L., and Hu, J.: Double high pollution events
580 in the Yangtze River Delta from 2015 to 2019: Characteristics, trends, and meteorological situations,
581 *Sci. Total Environ.*, 792, 10.1016/j.scitotenv.2021.148349, 2021.
- 582 Qu, Y., Wang, T., Yuan, C., Wu, H., Gao, L., Huang, C., Li, Y., Li, M., and Xie, M.: The underlying
583 mechanisms of PM_{2.5} and O₃ synergistic pollution in East China: Photochemical and
584 heterogeneous interactions, *Sci. Total Environ.*, 873, 162434,
585 <https://doi.org/10.1016/j.scitotenv.2023.162434>, 2023.
- 586 Rienda, I. C., and Alves, C. A.: Road dust resuspension: A review, *Atmos. Res.*, 261,
587 10.1016/j.atmosres.2021.105740, 2021.
- 588 Schwartz, S. E. In *Mass-Transport Considerations Pertinent to Aqueous Phase Reactions of Gases*
589 *in Liquid-Water Clouds, Chemistry of Multiphase Atmospheric Systems*, Jaeschke, W., Ed.
590 Springer Berlin Heidelberg: Berlin, Heidelberg, 1986; pp 415-471.



- 591 Shao, M., Wang, W., Yuan, B., Parrish, D. D., Li, X., Lu, K., Wu, L., Wang, X., Mo, Z., Yang, S., Peng,
592 Y., Kuang, Y., Chen, W., Hu, M., Zeng, L., Su, H., Cheng, Y., Zheng, J., and Zhang, Y.: Quantifying
593 the role of PM_{2.5} dropping in variations of ground-level ozone: Inter-comparison between Beijing
594 and Los Angeles, *Sci. Total Environ.*, 788, 147712, <https://doi.org/10.1016/j.scitotenv.2021.147712>,
595 2021.
- 596 Shao, M., Yang, J., Wang, J., Chen, P., Liu, B., and Dai, Q.: Co-Occurrence of Surface O₃, PM_{2.5}
597 Pollution, and Tropical Cyclones in China, *J Geophys. Res. Atmospheres*, 127, e2021JD036310,
598 <https://doi.org/10.1029/2021JD036310>, 2022.
- 599 Song, H., Lu, K., Dong, H., Tan, Z., Chen, S., Zeng, L., and Zhang, Y.: Reduced Aerosol Uptake of
600 Hydroperoxyl Radical May Increase the Sensitivity of Ozone Production to Volatile Organic
601 Compounds, *Environ. Sci. Technol. Lett.*, 9, 22-29, [10.1021/acs.estlett.1c00893](https://doi.org/10.1021/acs.estlett.1c00893), 2022.
- 602 Song, S., Ma, T., Zhang, Y., Shen, L., Liu, P., Li, K., Zhai, S., Zheng, H., Gao, M., Moch, J. M., Duan,
603 F., He, K., and McElroy, M. B.: Global modeling of heterogeneous hydroxymethanesulfonate
604 chemistry, *Atmos. Chem. Phys.*, 21, 457–481, <https://doi.org/10.5194/acp-21-457-2021>, 2021.
- 605 Vohra, K., Marais, E. A., Bloss, W. J., Schwartz, J., Mickley, L. J., Van Damme, M., Clarisse, L., and
606 Coheur, P.-F.: Rapid rise in premature mortality due to anthropogenic air pollution in fast-growing
607 tropical cities from 2005 to 2018, *Sci. Adv.*, 8, eabm4435-eabm4435, [10.1126/sciadv.abm4435](https://doi.org/10.1126/sciadv.abm4435),
608 2022.
- 609 Wang, S., Zhao, Y., Chan, A. W. H., Yao, M., Chen, Z., and Abbatt, J. P. D.: Organic Peroxides in Aerosol:
610 Key Reactive Intermediates for Multiphase Processes in the Atmosphere, *Chem. Rev.*,
611 [10.1021/acs.chemrev.2c00430](https://doi.org/10.1021/acs.chemrev.2c00430), 2023.
- 612 Wang, W., Liu, M., Wang, T., Song, Y., Zhou, L., Cao, J., Hu, J., Tang, G., Chen, Z., Li, Z., Xu, Z., Peng,
613 C., Lian, C., Chen, Y., Pan, Y., Zhang, Y., Sun, Y., Li, W., Zhu, T., Tian, H., and Ge, M.: Sulfate
614 formation is dominated by manganese-catalyzed oxidation of SO₂ on aerosol surfaces during haze
615 events, *Nat. Commun.*, 12, [10.1038/s41467-021-22091-6](https://doi.org/10.1038/s41467-021-22091-6), 2021.
- 616 Watson, J. G., Chow, J. C., and Houck, J. E.: PM_{2.5} chemical source profiles for vehicle exhaust,
617 vegetative burning, geological material, and coal burning in Northwestern Colorado during 1995,
618 *Chemo.*, 43, 1141-1151, [10.1016/s0045-6535\(00\)00171-5](https://doi.org/10.1016/s0045-6535(00)00171-5), 2001.
- 619 World Health Organization. WHO global air quality guidelines: particulate matter (PM_{2.5} and PM₁₀),



- 620 ozone, nitrogen dioxide, sulfur dioxide and carbon monoxide. 2021 (2021-12-21). ISBN 978-92-4-
621 003422-8
- 622 Wu, X., Xu, L. L., Hong, Y. W., Chen, J. F., Qiu, Y. Q., Hu, B. Y., Hong, Z. Y., Zhang, Y. R., Liu, T. T.,
623 Chen, Y. T., Bian, Y. H., Zhao, G. Q., Chen, J. S., and Li, M. R.: The air pollution governed by
624 subtropical high in a coastal city in Southeast China: Formation processes and influencing
625 mechanisms, *Sci. Total Environ.*, 692, 1135-1145, 10.1016/j.scitotenv.2019.07.341, 2019.
- 626 Wu, X., Li, M., Chen, J., Wang, H., Xu, L., Hong, Y., Zhao, G., Hu, B., Zhang, Y., Dan, Y., and Yu, S.:
627 The characteristics of air pollution induced by the quasi-stationary front: Formation processes and
628 influencing factors, *Sci. Total Environ.*, 707, 10.1016/j.scitotenv.2019.136194, 2020.
- 629 Wu, Y., Huo, J., Yang, G., Wang, Y., Wang, L., Wu, S., Yao, L., Fu, Q., and Wang, L.: Measurement report:
630 Production and loss of atmospheric formaldehyde at a suburban site of Shanghai in summertime,
631 *Atmos. Chem. Phys.*, 23, 2997-3014, 10.5194/acp-23-2997-2023, 2023.
- 632 Xiao, Q., Geng, G., Xue, T., Liu, S., Cai, C., He, K., and Zhang, Q.: Tracking PM_{2.5} and O₃ Pollution
633 and the Related Health Burden in China 2013-2020, *Environ. Sci. Technol.*, 56, 6922-6932,
634 10.1021/acs.est.1c04548, 2022.
- 635 Xu, R., Li, X., Dong, H., Lv, D., Kim, N., Yang, S., Wang, W., Chen, J., Shao, M., Lu, S., Wu, Z., Chen,
636 S., Guo, S., Hu, M., Liu, Y., Zeng, L., and Zhang, Y.: Field observations and quantifications of
637 atmospheric formaldehyde partitioning in gaseous and particulate phases, *Sci. Total Environ.*, 808,
638 10.1016/j.scitotenv.2021.152122, 2022.
- 639 Xue, L., Gu, R., Wang, T., Wang, X., Saunders, S., Blake, D., Louie, P. K. K., Luk, C. W. Y., Simpson,
640 I., Xu, Z., Wang, Z., Gao, Y., Lee, S., Mellouki, A., and Wang, W.: Oxidative capacity and radical
641 chemistry in the polluted atmosphere of Hong Kong and Pearl River Delta region: analysis of a
642 severe photochemical smog episode, *Atmos. Chem. Phys.*, 16, 9891-9903, 10.5194/acp-16-9891-
643 2016, 2016.
- 644 Zhang, K., Duan, Y., Huo, J., Huang, L., Wang, Y., Fu, Q., Wang, Y., and Li, L.: Formation mechanism
645 of HCHO pollution in the suburban Yangtze River Delta region, China: A box model study and
646 policy implementations, *Atmos. Environ.*, 267, 118755,
647 <https://doi.org/10.1016/j.atmosenv.2021.118755>, 2021.
- 648 Zhang, N., Guan, Y., Jiang, Y., Zhang, X., Ding, D., and Wang, S.: Regional demarcation of synergistic



649 control for PM_{2.5} and ozone pollution in China based on long-term and massive data mining, *Sci.*
650 *Total Environ.*, 155975, <https://doi.org/10.1016/j.scitotenv.2022.155975>, 2022.

651 Zhao, D., Liu, G., Xin, J., Quan, J., Wang, Y., Wang, X., Dai, L., Gao, W., Tang, G., Hu, B., Ma, Y., Wu,
652 X., Wang, L., Liu, Z., and Wu, F.: Haze pollution under a high atmospheric oxidization capacity in
653 summer in Beijing: insights into formation mechanism of atmospheric physicochemical processes,
654 *Atmos. Chem. Phys.*, 20, 4575-4592, [10.5194/acp-20-4575-2020](https://doi.org/10.5194/acp-20-4575-2020), 2020.

655 Zong, L., Yang, Y., Gao, M., Wang, H., Wang, P., Zhang, H., Wang, L., Ning, G., Liu, C., Li, Y., and Gao,
656 Z.: Large-scale synoptic drivers of co-occurring summertime ozone and PM_{2.5} pollution in eastern
657 China, *Atmos. Chem. Phys.*, 21, 9105-9124, [10.5194/acp-21-9105-2021](https://doi.org/10.5194/acp-21-9105-2021), 2021.